Preparation of hydroxyapatite-based porous materials for absorption of lead ions

Zejun Wang, Kangqi Sun, Yufeng He, Pengfei Song, Dawei Zhang and Rongmin Wang

ABSTRACT

In this paper, soybean protein isolate (SPI) was used as template, hydroxyapatite was crystallized on protein chains of SPI by in-situ synthesis, then the obtained inorganic HA/biopolymer SPI composite (HA@SPI) was calcined at suitable temperature, which afforded a novel hydroxyapatite-based porous materials (HApM). The results indicated that the product showed a porous morphology structure and excellent absorption performance for Pb^{2+}. HApM maximum removal of lead was attained (96.25%) at an initial pH value of 7.4, temperature of 25 °C and contact time of 30 min with an initial metal concentration of 60 mg/L. In order to identify composition, structure and functional groups involved in the uptake of Pb^{2+}, Fourier transform infrared spectrometer (FTIR), thermogravimetric analysis (TG), X-ray diffraction (XRD) scanning electron microscopy (SEM), energy dispersive spectroscopy (EDS), and Brunauer–Emmett–Teller (BET) analysis were carried out. Therefore, the hydroxyapatite-based porous materials (HApM) is a promising candidate for the treatment of liquid wastes containing toxic Pb^{2+} metal ion, heavy metal ion antidotes and other related fields.

Key words | biocompatible porous materials, hydroxyapatite-based composites, Pb^{2+} adsorption, soy protein isolate

Zejun Wang
Kangqi Sun
Yufeng He
Pengfei Song
Dawei Zhang
Rongmin Wang (corresponding author)
Key Laboratory of Eco-functional Polymer Materials of the Ministry of Education, Institute of Polymer, College of Chemistry and Chemical Engineering,
Northwest Normal University,
Lanzhou 730070,
China
E-mail: wangrm@nwnu.edu.cn

INTRODUCTION

Hydroxyapatite (HA) is the main inorganic constituent of vertebrate hard tissues such as bones and teeth, which has been chosen to study the system of biomolecule/biocompatible-surface interactions (Rimola et al. 2008). As the major constituent of bone (Akram et al. 2014; Liu et al. 2016), HA was coupled with inorganics (Fu et al. 2015; Anitha et al. 2017) and organics (Lv et al. 2013; Lin et al. 2016) for bone tissue engineering application. Since excellent biocompatibility, biodegradability, non-toxicity and high stability, it was extensively used in biomedical fields including dental restoration (Lee et al. 2017), controlling transport of proteins (Zhu et al. 2017), genes (Escudero et al. 2013; Deshmukh et al. 2016) and other applications (Fujita et al. 2016; Zhang et al. 2017). Furthermore, HA materials are of great significance in many other fields such as removing harmful volatile organic compounds (VOCs) (Fang et al. 2016), fuel cells (Wei & Matthew 2012) and corrosion inhibitors (Snihirova et al. 2010).

Due to Ca^{2+} exchange performance, HA has adsorption and immobilization effect on metal ions, such as Cd^{2+}, Pd^{2+}.

Because of this feature, HA has been successfully used in heavy metal-contaminated soil (Wei et al. 2016) and water treatment (Meski et al. 2011; Wijesinghe et al. 2018). To improve absorption efficiency, biopolymer-hydroxyapatite composite was employed to remove heavy metals from aqueous solutions. Vila et al. (2011) have developed 3D-macroporous biopolymer-coated hydroxyapatite (HA) foams as potential devices for the treatment of Pb^{2+}, cadmium and copper contamination of consumable water (Vila et al. 2011). Narwade et al. (2018) used in-situ synthesis method to prepare hydroxyapatite in the presence of cellulose nanofibrils (CNF) or TEMPO-oxidized CNF (TCNF) by wet chemical precipitation process, which combined with a low-cost biosorbent to remove heavy metal ion. Moreover, scientists found that HA particles with different morphologies, such as fibrous, plate-like, agglomerate-like, rodlike, needle-like and spherical, highly affected the efficiency of remove heavy metal ions (Qi et al. 2016; Wang et al. 2016).

The absorbent's surface structure and morphology deeply influence remove rate. We found that polymer

modified inorganic clay could efficiently remove heavy metal ions (He *et al.* 2012), and plant-protein-modified semiconductor photocatalyst increased activity in photo-degradation of dyes (Wang *et al.* 2018). Recently, increasing emphases were turned to natural polymers in the development of environmentally-friendly products (Wang *et al.* 2017; Al-Othman *et al.* 2012; Naushad & ALOthman 2015). As the soy protein isolate (SPI) with reproducible resource was used as template, this work could provide an efficient new treatment without high cost. In addition, HA and SPI are multifunctional biomaterials with biocompatibility and environmental friendliness. Herein, we prepared a novel HA-based hybrid with special structure and morphology by using SPI as bio-template. The obtained hybrid material was used as adsorbent to remove heavy metal ions from aqueous solutions to investigate its adsorption property. The influence of time, initial concentration of heavy metal ions, and the amount of adsorbent was tested. These hybrids have been studied in terms of isotherm models and sorption kinetics analysis at neutral medium in order to consider their application as heavy metal removers from aqueous solutions.

MATERIALS AND METHODS

Materials

SPI (Shanghai Yuanye Bio-Technology Co. Ltd), urea (Tianjin Zhiyuan Chemical Reagent Co., Ltd), $(NH_4)_2HPO_4$ (Shanghai Zhongqin Chemical Co., Ltd), $Ca(NO_3)_2$ (Tianjin Kexin Chemical Industry Co., Ltd), and $Pb(NO_3)_2$ (Tianjin Daming Chemical Reagent Factory) were obtained commercially and used without further purification. Distilled water was used in all experiments.

Preparation of HApM hybrids

In 20 mL of urea solution (8 mol/L), 1.000 g SPI was dissolved by stirring at room temperature, and then stirred for 12 hrs. Subsequently, the SPI solution was treated for 4 h and denatured in a heating bath at 90 °C. After adding 5 mL of $(NH_4)_2HPO_4$ aqueous solution (1.195 mol/L), the mixture was stirred for 30 min. Next, 5 mL of $Ca(NO_3)_2$ aqueous solution (1.952 mol/L) was added dropwise into the mixture. Subsequently, adjusting pH value to 7.4 by the ammonia, the mixture was reacted for 3 h with stirring at 90 °C. Then, the system was continued to stir for 12 h at 25 °C. The product was centrifugally separated, and washed with distilled water for removing urea. After freeze-drying, HA@SPI composite was obtained.

The HA@SPI composites obtained by 3 g were calcined at the temperatures of 200 °C, 400 °C, 500 °C, 600 °C, 700 °C, 800 °C for 60 min by temperature-programmed calcination in muffle furnace to afford the hybrids and was named as SPI/HA-200, SPI/HA-400, PI/HA-500, SPI/HA-600 (HApM), SPI/HA-700, SPI/HA-800, respectively (Figure S1, Supplementary Information). The result showed that HApM (calcined at 600 °C) showed the best adsorption ability.

Characterizations

Fourier transform infrared (FTIR) spectra of the adsorbents were recorded between 4,000 and 400 cm^{-1} through the KBr method with a FTS3000 spectrophotometer (FTS3000, DigiLAB Merlin, USA). Thermogravimetric analysis (TGA) was carried out at a condition of N_2 protection and temperature range being 25 °C–800 °C, heating rate being 10 °C/min (PerkinElmer, model Pyris Diamond, USA). The crystal structures and photocurrent responses were characterized by X-ray diffraction (XRD) (D/max-2400, Rigaku Corporation, Japan). A morphology analysis of certain features was visualized by using scanning electron microscopy (SEM) (ULTRA PLUS, ZEISS, Germany).

Adsorption performance of HApM hybrid

The Pb^{2+} were desorbed from HA, SPI, HA@SPI and HApM by shaking them in a 50 mL Pb^{2+} solution at a temperature of 25 °C and a speed of 125 rpm, respectively. After the adsorption process, the adsorbent was separated from the samples by filtering. Filtrate was analyzed by UV-Vis (Agilent 8,453, Agilent Technologies, USA). Parameters affecting the adsorption process, such as adsorbent dosage, initial Pb^{2+} concentration, contact time were studied. The removal rate and adsorption capacity were computed as following equations.

$$Removal\% = \left(\frac{C_0 - C_e}{C_0}\right) \times 100\% \qquad (1)$$

$$Adsorption\ capacity = \frac{(C_0 - C_e)}{m}V \qquad (2)$$

where C_0 and C_e are the initial and equilibrium concentration of metal ions (mg/L) in the solution, respectively. V is the volume of metal ions solution (L), m is the weight of the adsorbent (g).

RESULTS AND DISCUSSION

As we know, SPI is a kind of edible, low-cost and plant-based protein whose chains show a loop domain containing several helices structure (Maruyama *et al.* 2004). Here, using SPI as biopolymer template, the microcrystal of hydroxyapatite was crystallized along with loop protein chains and HA@SPI composite was synthesized. Subsequently, the HA@SPI was calcined at 600 °C, in the process of calcination, hydroxyapatite was mineralized and a part of SPI was carbonized. Finally, HA based hybrids (HApM) were successfully prepared (Figure 1).

IR analysis

The obtained hydroxyapatite-based porous materials (HApM) were characterized by FTIR spectra, and compared with HA@SPI, templates materials (SPI), pure HA, and SPI/HA-Tx (Figure S2, Supplementary Information). The results are shown in Figure 2. It indicates that HA@SPI displayed characteristic absorption peaks both of SPI (1,649 cm^{-1}, 1,535 cm^{-1} and 1,244 cm^{-1} are corresponding to -CONH-) and HA (PO_4^{3-} vibration bands at 1,033, 603, and 566 cm^{-1} and -OH band at 3,441 cm^{-1}). Characteristic absorption peaks of HApM are similar to HA@SPI, but the peaks of HA in HApM are more obvious. The amide two new characteristic peaks appeared at 2,050 cm^{-1} and 2,450 cm^{-1} which could be caused by carbonization. These results indicated that SPI of HA@SPI was turned to activated carbon at heating condition, and hydroxyapatite-based porous material was obtained (HApM). At the same time, a sharp peak at 1,628 cm^{-1} corresponded to H–O–H bending band, being also representative of the strongly bonded –OH groups in the matrix. The O–H stretching bands merged together and shifted to lower frequency in the spectra of HApM. This was due to the possibility of H-bonding. It is also apparent from Figure 2 that after adsorption of Pb²⁺ (HApM-after), the intensity and position of

1,628 cm^{-1} peak was changed, and the intensity of the 3,441 cm^{-1} peak weakens slightly, which demonstrated the involvement of –OH groups in the adsorption of Pb²⁺.

TG analysis

TG curves are shown in Figure 3. Compare HA@SPI with SPI and pure HA, main weight loss of HA@SPI is due to SPI degradation, but for SPI itself, there was 22% remained at 800 °C which was according the degradation of SPI, its carbonization product. And it also can be deduced that the proportion of HA and SPI is 1:1. Although the calculated temperature was as high as 800 °C, the weight of HA@SPI is only 1.5% which owed to further carbonization of HA@SPI. These results suggested that the main interaction in preparing HApM progress was due to SPI carbonization of HA@SPI (Figure S3, Supplementary Information).

XRD analysis

The XRD patterns of biopolymer-template SPI, pure HA, composite HA@SPI and HApM were given in Figure 4. It can be observed from the figure that when 2θ is 32°, the powder of SPI/HA-200, SPI/HA-400, SPI/HA-500, SPI/HA-600 and SPI/HA-800 all have (211) crystal plane diffraction peak, and when it is near 25°, The diffraction peak of (002) crystal plane appears, which is the most important characteristic diffraction peak of HA, indicating that SPI/HA, SPI/HA-200, SPI/HA-400, SPI/HA-500, HApM and SPI/HA-800 all formed HA crystals. At the same time, it can be seen from the diagram that the diffraction peaks of (102), (210), (300) and (202) planes tend to be sharp with the increase of calcination temperature, and the diffraction peaks of each crystal plane of SPI/HA-800 are sharp. The position and intensity are consistent with the characteristic diffraction peak of HA, indicating that the crystallization degree of HA in SPI/HA-800 complex is the best and the purity of the product is very high (Figure S4, Supplementary Information).
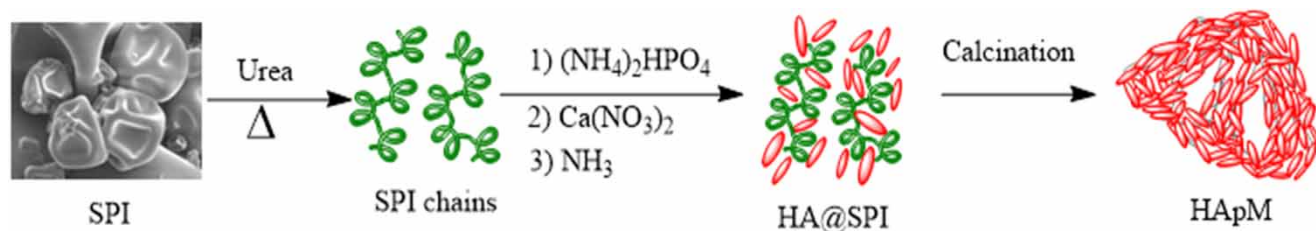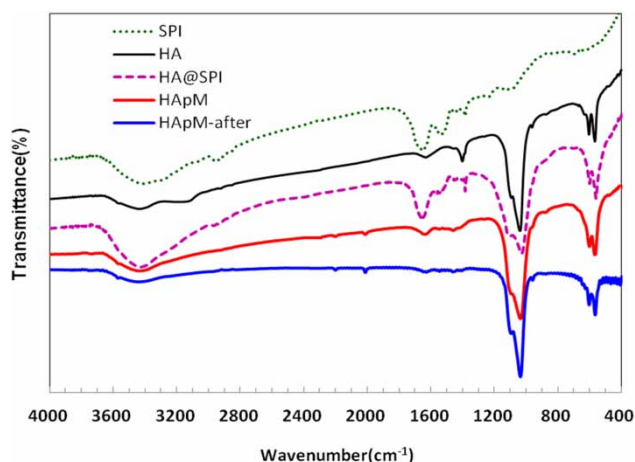

Figure 1 | Preparation of HA@SPI and HApM.

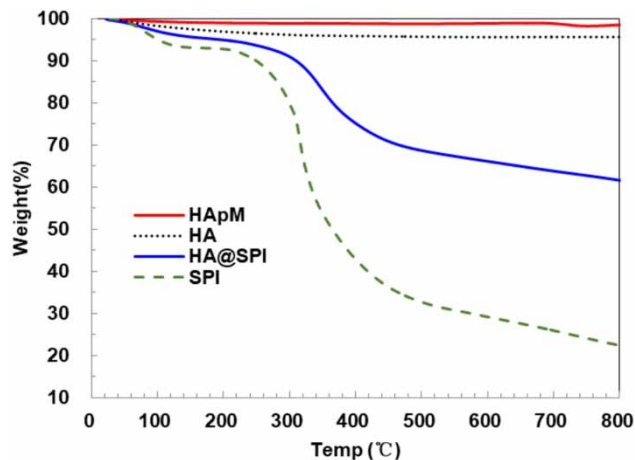**Figure 2** | FTIR spectra of HA, SPI, HA@SPI, HApM and HApM-after.

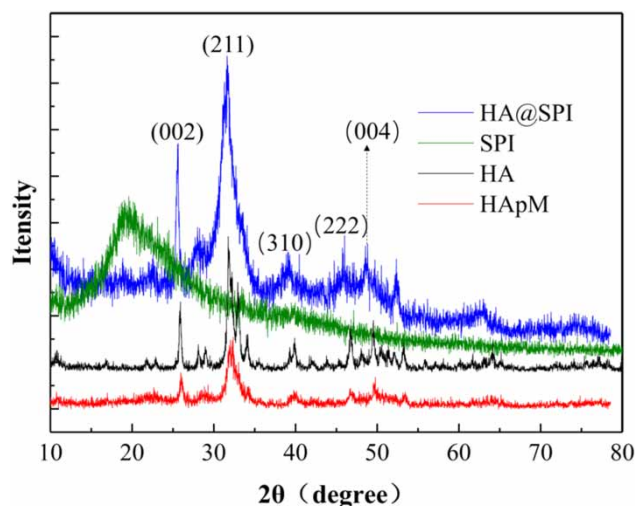**Figure 3** | TG curves of HA, SPI, HA@SPI and HApM.

Figure 4 | XRD patterns of HA, SPI, HA@SPI and HApM.

SEM-EDS images

By observing the morphology of SPI/HA-200, SPI/HA-400, SPI/HA-500, HApM, SPI/HA-700 and SPI/HA-800 under scanning electron microscope (as shown in Figure S5, Supplementary Information), it can be seen that when the calcination temperature is 200 °C, the morphology of the composite SPI/HA-200 is close to that of HA@SPI, but the pore size increases slightly. When the calcination temperature is 400 °C, 500 °C and 600 °C, the pores of SPI/HA-400, SPI/HA-500 and HApM continue to increase, and there are different degrees of agglomeration at the same time. With the increase of temperature, when the calcination temperature rises to 700 °C, the pores of the composite SPI/HA-700 collapse and have obvious agglomeration, and the microscopic morphology is closer to that of HA. When the calcination temperature rises to 800 °C, the SPI/HA-800 agglomeration of the composite is serious. From the microscopic morphology of SPI/HA-Tx series, it can be seen that the SPI in the composite is gradually degraded with the increase of calcination temperature, which is consistent with the results of TG analysis. When the calcination temperature is 600 °C, the pore structure of SPI/HA-600(HApM) is the best. At the same time, the SEM pictures of HApM before and after adsorption of Pb^{2+} were compared. It was found that after the adsorption of Pb^{2+} ions, the porous morphology of HApM was filled in different degrees because of the adsorption of Pb^{2+} on the surface and pores. The energy dispersive spectroscopy (EDS) elemental analysis of HApM after adsorption of Pb^{2+} was carried out, and the results were verified (Figure 5).

BET analysis

The Brunauer–Emmett–Teller (BET) specific surface area (S_{BET}) and pore-size distribution of the products were investigated. As shown in Figure 6(a) and 6(b), the specific surface area of HApM is 123.954 m^2/g, which is higher than that of HApM-after (118.317 m^2/g). The results show that due to the adsorption of Pb^{2+} on the surface and pores of HApM porous materials, the specific surface product of Pb^{2+} adsorbed decreases. The results were in good agreement with EDS analysis.

Adsorption

Heavy metal ions in water can cause long-term and serious harm to people and the environment. In particular, Pb^{2+} can lead to endocrine and reproductive system disorders,
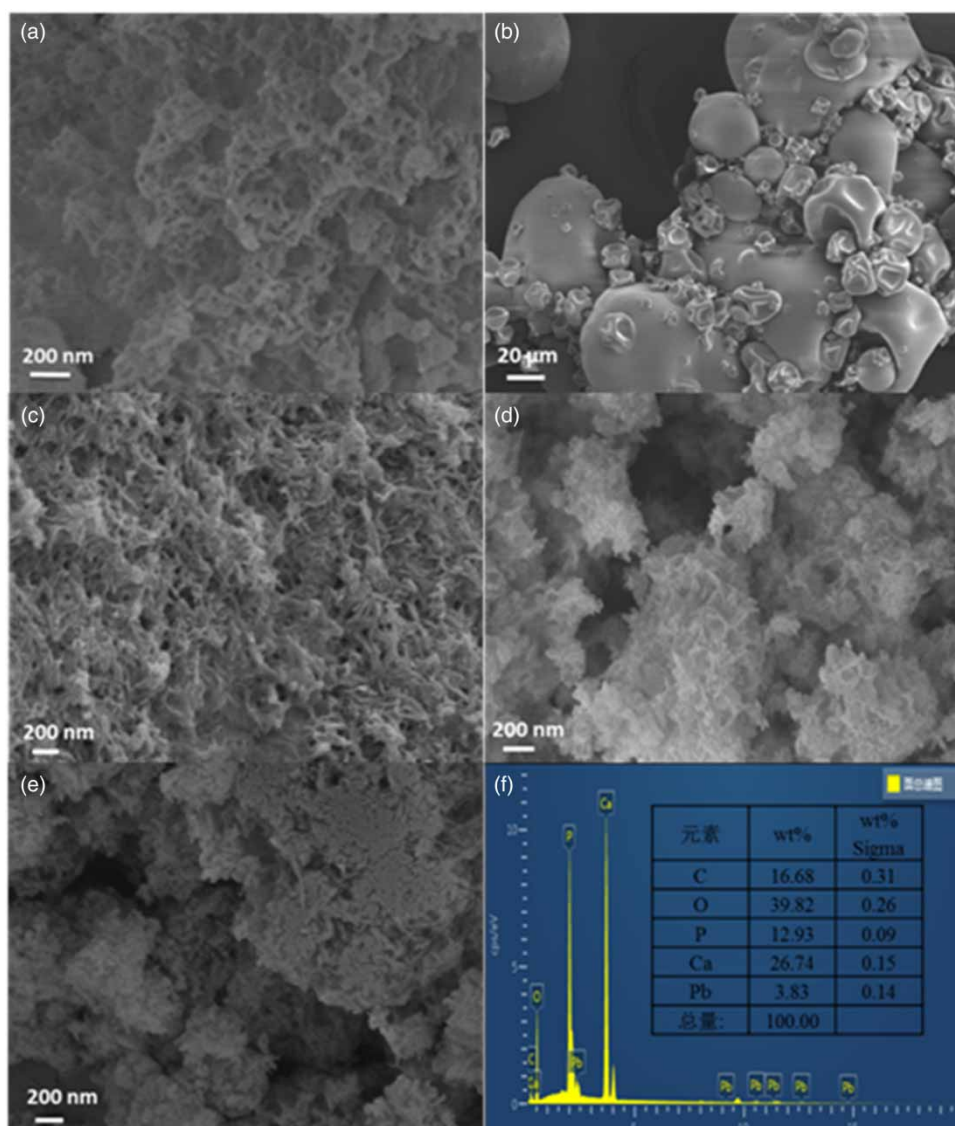
Figure 5 │ SEM images of (a) HA, (b) SPI, (c) HA@SPI, (d) HApM, (e) HApM after adsorption of Pb^{2+} and EDX spectra image of (f) HApM after adsorption of Pb^{2+}.

teratogenicity and even carcinogenesis. Here, we used Pb^{2+} as model heavy metal ion, the respective adsorption ability of HA, SPI, HA@SPI and HApM were evaluated and shown in Table 1. The results showed that removal efficiency of Pb^{2+} by HApM was higher than HA, SPI and HA@SPI which implied that HAPM was an effective adsorbent.

Optimization of the adsorption conditions of HApM

To investigate influence of adsorption conditions, the amount of adsorbent (HApM) (0.2, 0.1 and 0.05 g), adsorption time (30, 60 and 90 min), initial concentration of Pb^{2+} (30, 50, 60 mg/L) were selected. Removal rate (%) and adsorption capacity (mg/g) were calculated by orthogonal adsorption experiments. As shown in Table 2, in the condition of adsorbent dosage was 0.1 g, initial concentration of Pb^{2+} was 60 mg/L and adsorption time was 30 min, the adsorbent achieved its maximum adsorption efficiency of 96.25% removal rate and 28.88 mg/g adsorption capacity. If the adsorption capacity was taken into account, the removal rate (90.02%) and the adsorption capacity (45.01 mg/g) were relatively high in the condition of 0.05 g adsorbent, 50 mg/L initial concentration of Pb^{2+} and 60 min adsorption time.
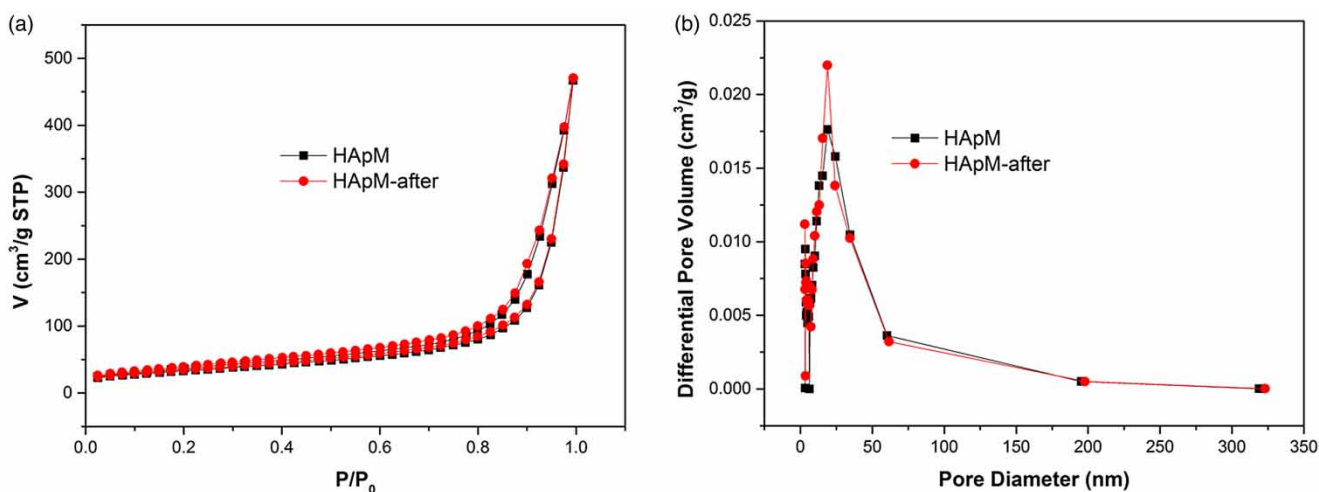
Figure 6 │ BET image of (a) HApM, (b) HApM after adsorption of Pb^{2+}.

Table 1 │ Adsorption ability of HA, SPI, HA@SPI and HApM in the removal of Pb^{2+}

Adsorbent	$[Pb^{2+}]_{Removal}$ (%)	Adsorption capacity (mg/g)
HApM	96.25	28.88
HA@SPI	77.20	19.28
HA	82.54	20.63
SPI	8.54	2.13

Table 2 │ Orthogonal experiments of HApM about adsorbing Pb^{2+}

No.	Adsorbent (g)	$[Pb^{2+}]_{Initial}$ (mg/L)	Time (min)	Removal (%)	Adsorption capacity (mg/g)
1	0.05	30	30	75.15	22.54
2	0.1	30	60	77.51	11.63
3	0.2	30	90	78.80	5.91
4	0.05	50	60	90.02	45.01
5	0.1	50	90	67.54	16.89
6	0.2	50	30	88.38	11.05
7	0.05	60	90	81.63	48.98
8	0.1	60	30	96.25	28.88
9	0.2	60	60	81.63	12.25

Adsorption isotherm and kinetics

Adsorption isotherm Langmuir and Freundlich isotherm models were applied to establish the relationship between the amounts of Pb^{2+} adsorbed onto adsorbent and its equilibrium concentration in aqueous solution. The Langmuir adsorption isotherm was applied to equilibrium adsorption assuming monolayer adsorption onto a surface of the adsorbent, and adsorption occurs at finite number of identical sites within the adsorbent. The Langmuir isotherm was described as Equation (3). The Freundlich model stipulates that the ratio of solute adsorbed to the solute concentration was a function of the solution. The empirical model was shown to be consistent with exponential distribution of active center, characteristic of heterogeneous surfaces (Equation (4)).

$$\frac{C_e}{q_e} = \frac{1}{q_{max}K_L} + \frac{C_e}{q_{max}} \tag{3}$$

$$\lg q_e = \lg K_F + \frac{1}{n}\lg C_e \tag{4}$$

where C_e is adsorption equilibrium concentration of adsorbate in solution (mg/L); q_e is adsorption capacity (mg/g) per unit mass of adsorbent at equilibrium; q_m is the maximum amount of monolayer adsorption per unit mass of adsorbent (mg/g); K_a is Langmuir isothermal adsorption energy constant (L/mg), K_F is Freundlich isothermal adsorption empirical constant, which related to adsorption capacity and adsorption intensity.

As shown in Table 3 and Figure 7, the parameters of Langmuir and Freundlich for the adsorption of Pb^{2+} by the HApM hybrid are obtained, which is 0.9616 and 0.9853 for Langmuir and Freundlich. It can be concluded that the Freundlich isotherm is more suitable to describe the adsorption processes of Pb^{2+} onto HApM than the Langmuir isotherm. In addition, the adsorption index $1/n$ of this experiment is 0.4282, which is between 0.1 and 0.5, indicating that HApM is easy to adsorb Pb^{2+}.

Table 3 | Parameters of Langmuir and Freundlich isotherms

Adsorption isotherms Langmuir	Parameter	Adsorption isotherms Freundlich	Parameter
q_m (mg/g)	28.1690	K_F [(mg/g) (L/g)/n]	5.3134
K_a (dm³/mg)	0.1211	1/n	0.4282
R^2	0.9616	R^2	0.9853

Adsorption kinetics

Adsorption kinetics was used to explain the adsorption mechanism and adsorption characteristics. Pseudo-first-order model is rendered as the rate of occupation of the adsorption sites to be proportional to the number of unoccupied sites; pseudo-second-order kinetic model is assumed the chemical reaction mechanisms, and that the adsorption rate is controlled by chemical adsorption through sharing or exchange of electrons between the adsorbate and adsorbent (Naushad *et al.* 2017). Here, the pseudo-first-order and pseudo-second-order kinetic models have been employed to fit the experimental data. The pseudo-first-order model and pseudo-second-order kinetic model can be explained by Equations (5) and (6).

$$\log(q_e - q_t) = \log q_e - \frac{k_1}{2.303}t \qquad (5)$$

$$\frac{t}{q_t} = \frac{1}{k_2 q_e^2} + \frac{t}{q_e} \qquad (6)$$

where q_e and q_t (mg/g) are the amount of Pb²⁺ adsorbed per unit mass of adsorbent at the equilibrium adsorption

and at time period t (min), and k_1 (min⁻¹), k_2 (g/m/min) are the first-order kinetic and pseudo-second-order rate constant.

As shown in Table 4 and Figure 8, the R^2 of the pseudo-first-order and pseudo-second-order kinetic parameters is 0.9269 and 0.9984, respectively. Moreover, the values of q_e (25.84 mg/g) calculated from pseudo-second-order kinetics are in agree with the experimental values of q_e(exp) (25.18 mg/g). It indicates that the pseudo-second-order model is appropriate for the adsorption phenomena, and chemical adsorption plays a major role in the adsorption process.

Mechanism of HApM and comparison with reported adsorbents

Based on above results, we considered it belongs to chemisorption. After absorption of Pb²⁺, HApM-after was characterized by SEM, FTIR and BET, and results are shown in Figures 2, 5 and 6, respectively. Comparing with HApM, in HApM-after (Figure 2), the intensity and position of 1,628 cm⁻¹ peak was changed, and the intensity of the 3,441 cm⁻¹ peak weakens slightly that demonstrated the involvement of –OH groups in the adsorption of Pb²⁺. From SEM images, it was found that, the surface morphology of HApM changed after adsorption of Pb²⁺ ions (Figure 5(e)). BET analysis also confirmed that the surface area of HApM decreased due to the adsorption of lead ion on the surface of HApM (Figure 6). Therefore, we speculated that lead ions react
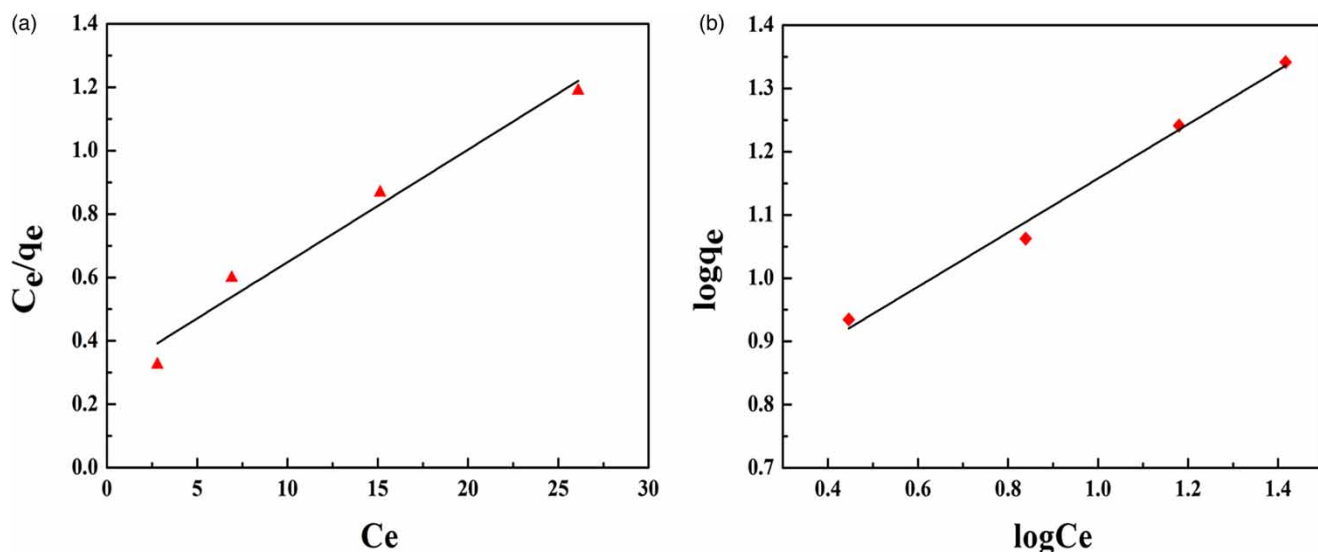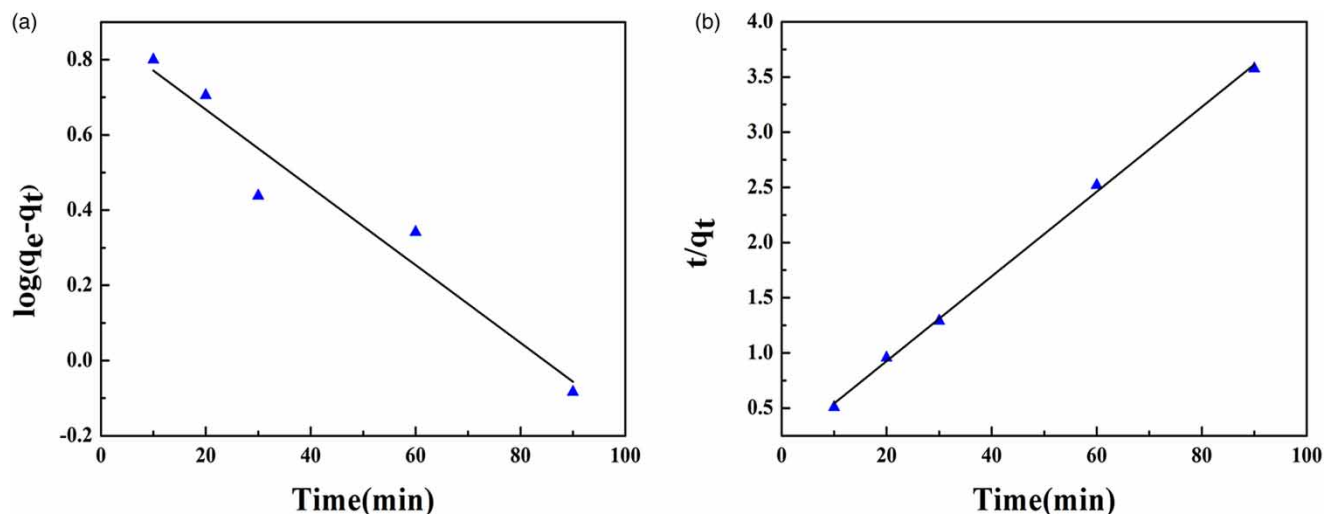

Figure 7 | Langmuir and Freundlich isotherms for removal of Pb²⁺ by HApM. (a) Langmuir adsorption isotherm, (b) Freundlich adsorption isotherm.

Table 4 | Parameters of pseudo-first and second-order kinetic models

		Pseudo-first-order kinetics model			Pseudo-second-order kinetics model		
C_0 (mg/L)	q_e, exp (mg/g)	q_e (mg/g)	k_1 (min⁻¹)	R^2	q_e (mg/g)	k_2[g/(mg min)]	R^2
60	25.18	7.4887	0.02381	0.9269	25.8398	0.00946	0.9984

Figure 8 | Kinetic models for Pb²⁺ ions (a) pseudo-first-order, (b) pseudo-second-order.

with hydroxyl groups so that lead ions were firmly adsorbed on the surface of hydroxyapatite.

The adsorption HApM was also compared with reported results (Table 5) (Mittal et al. 2016; Naushad 2014; Gnanasekaran et al. 2018; Pugazhendhi et al. 2018). Ghasemi et al. (2014a; 2014b) reported that the Ash, nFe-A and FSAC adsorbents have excellent adsorption capacity of Pb²⁺.

Table 5 | Comparison of maximum monolayer adsorption capacities for Pb²⁺ removal

	Optimum condition				
Adsorbents	pH	Temp (°C)	Adsorption time	Removal of Pb²⁺ (%)	q_{max} (mg/g)
KTSMBNL 13	7.0	35	26 h	90.0	–
SDS-AZS	6.0	25	40 min	90.5	21.01
Ash	6.0	25	40 min	89.0	588.24
nFe-A	6.0	25	40 min	94.0	833.33
FSAC	4.0	25	60 min	95.8	80.645
TIV	6.0	20–55	60 min	95.0	18.8
MWCNTs/ThO₂	5.5	45	50 min	94.6	–
PVA/HAp	5.5	30	40 min	95.9	7.99
HApM	7.4	25	30 min	96.3	28.88

Separately, and the maximum adsorption capacities are 588.24 mg/g, 833.33 mg/g, 80.645 mg/g. Naushad et al. (2015) found that the removal of Pb²⁺ got to 95% using TIV as adsorbent, and the maximum adsorption capacity was 18.8 mg/g. Le et al. (2019) used porous hydroxyapatite granules as an effective adsorbent for the Removal of Aqueous Pb(II) Ions which the removal of Pb²⁺ got to 95.9%, and the maximum adsorption capacity was 7.99 mg/g. Here, using HApM as adsorbent, the removal of lead got to 96.25%, while the adsorption capacity was 28.88 mg/g.

CONCLUSION

In summary, a kind of HA based hybrid has been successfully fabricated and tested as Pb²⁺ removers from aqueous solutions. Morphology and structure of the HApM suggest that protein chains were shank and carbonized in the calcined process and formed a highly porous HA based hybrid which have proved an excellent adsorption capacity of 96.25% for Pb²⁺. The adsorption data fitted well with Freundlich isotherm model, and being followed by the chemisorption according to the pseudosecond-order. All of those suggest that the HA based hybrid will be an ideal

Pb²⁺ adsorbent for the treatment of liquid wastes containing toxic Pb²⁺ metal ion, which could provide high effectiveness with low-cost and environmental friendliness.

ACKNOWLEDGEMENTS

SUPPLEMENTARY MATERIAL

The Supplementary Material for this paper is available online at http://dx.doi.org/10.2166/wst.2019.370.

REFERENCES

Akram, M., Ahmed, R., Shakir, I., Ibrahim, W. A. W. & Hussain, R. 2014 Extracting hydroxyapatite and its precursors from natural resources. *Journal of Materials Science* **49**, 1461–1475.

Al-Othman, Z. A., Ali, R. & Naushad, M. 2012 Hexavalent chromium removal from aqueous medium by activated carbon prepared from peanut shell: adsorption kinetics, equilibrium and thermodynamic studies. *Chemical Engineering Journal* **184**, 238–247.

Anitha, A., Menon, D., Sivanarayanan, T. B., Koyakutty, M., Mohan, C., Shantikumar, V. N. & Manitha, B. N. 2017 Bioinspired composite matrix containing hydroxyapatite-silica core-shell nanorods for bone tissue engineering. *ACS Applied Materials & Interfaces* **9**, 26707–26718.

Deshmukh, K., Shaik, M. M., Ramanan, S. R. & Kowshik, M. 2016 Self-activated fluorescent hydroxyapatite nanoparticles: a promising agent for bioimaging and biolabeling. *ACS Biomaterials Science & Engineering* **2**, 1257–1264.

Escudero, A., Mauricio, E. C., Fernandez, S. R., Fuente, J. M. D. L. & Ocaña, M. 2013 Microwave-assisted synthesis of biocompatible europium-doped calcium hydroxyapatite and fluoroapatite luminescent nanospindles functionalized with poly(acrylic acid). *Langmuir* **29**, 1985–1994.

Fang, B. B., Yan, Y. B., Yang, Y., Wang, F. L., Chu, Z., Sun, X. Y., Li, J. S. & Wang, L. J. 2016 Adsorption of Pb²⁺ from aqueous solution using spinel ferrite prepared from steel pickling sludge. *Water Science & Technology* **73** (5), 1112.

Fu, C., Savino, K., Gabrys, P., Zeng, A. B., Guan, B. H., Olvera, D., Wang, C. G., Song, B. A., Awad, H., Gao, Y. L. & Yates, M. Z. 2015 Hydroxyapatite thin films with giant electrical polarization. *Chemistry of Materials* **27**, 1164–1171.

Fujita, H., Kudo, T. A., Kanetaka, H., Miyazaki, T., Hashimoto, M. & Kawashita, M. 2016 Adsorption of laminin on hydroxyapatite and alumina and the MC3T3-E1 cell response. *ACS Biomaterials Science & Engineering* **2**, 1162–1168.

Ghasemi, M., Naushad, M., Ghasemi, N. & Khosravi-Fard, Y. 2014a Adsorption of Pb (II) from aqueous solution using new adsorbents prepared from agricultural waste: adsorption isotherm and kinetic studies. *Journal of Industrial and Engineering Chemistry* **20** (4), 2193–2199.

Ghasemi, M., Naushad, M., Ghasemi, N. & Khosravi-Fard, Y. 2014b A novel agricultural waste based adsorbent for the removal of Pb (II) from aqueous solution: kinetics, equilibrium and thermodynamic studies. *Journal of Industrial and Engineering Chemistry* **20** (2), 454–461.

Gnanasekaran, L., Hemamalini, R. & Naushad, M. 2018 Efficient photocatalytic degradation of toxic dyes using nanostructured TiO₂/polyaniline nanocomposite. *Desalination and Water Treatment* **108**, 322–328.

He, Y.-H., Zhang, L., Wang, R.-M., Li, H.-R. & Wang, Y. 2012 Loess clay based copolymer for removing Pb(II) ions. *Journal of Hazardous Materials* **227**, 334–340.

Le, D. T., Le, T. P. T., Do, H. T., Vo, H. T., Pham, N. T., Nguyen, T. T. & Tran, D. L. 2019 Fabrication of porous hydroxyapatite granules as an effective adsorbent for the removal of aqueous Pb (II) ions. *Journal of Chemistry* **2019**, 1–10.

Lee, H. S., Myers, C., Zaidel, L., Nalam, P. C., Caporizzo, M. A., Daep, C. A., Eckmann, D. M., Masters, J. G. & Composto, R. J. 2017 Competitive adsorption of polyelectrolytes onto and into pellicle-coated hydroxyapatite investigated by QCM–D and force spectroscopy. *ACS Applied Materials & Interfaces* **9**, 13079–13091.

Lin, K. F., He, S., Song, Y., Wang, C. M., Gao, Y., Li, J. Q., Tang, P., Wang, Z., Bi, L. & Pei, G. X. 2016 Low-temperature additive manufacturing of biomimic three dimensional hydroxyapatite/collagen scaffolds for bone regeneration. *ACS Applied Materials & Interfaces* **8**, 6905–6916.

Liu, C., Zhai, H. L., Zhang, Z. S., Li, Y. l., Xu, X. R. & Tang, R. K. 2016 Cells recognize and prefer bone-like hydroxyapatite: biochemical understanding of ultrathin mineral platelets in bone. *ACS Applied Materials & Interfaces* **8**, 29997–30004.

Lv, L. X., Zhang, X. F., Wang, Y. Y., Ortiz, L., Mao, X., Jiang, Z. L., Xiao, Z. D. & Huang, N. P. 2013 Effects of hydroxyapatite-containing composite nanofibers on osteogenesis of mesenchymal stem cells in vitro and bone regeneration In vivo. *ACS Applied Materials & Interfaces* **5**, 319–330.

Maruyama, Y., Maruyama, N., Mikami, B. & Utsumi, S. 2004 Structure of the core region of the soybean β-conglycinin α'subunit. *Acta Crystallographica Section D-Structural Biology* **60** (2), 289–297.

Meski, S., Ziani, S., Khireddine, H., Yataghane, F. & Ferguene, N. 2011 Elaboration of the hydroxyapatite with different precursors and application for the retention of the Pb²⁺. *Water Science & Technology* **63** (10), 2087–2096.

Mittal, A., Naushad, M., Sharma, G., ALothman, Z. A., Wabaidur, S. M. & Alam, M. 2016 Fabrication of MWCNTs/ThO₂ nanocomposite and its adsorption behavior for the removal of Pb (II) metal from aqueous medium. *Desalination and Water Treatment* **57** (46), 21863–21869.

Narwade, V. N., Khairnar, R. S. & Kokol, V. 2018 In situ synthesized hydroxyapatite – cellulose nanofibrils as

biosorbents for heavy metal ions removal. *Journal of Polymers and the Environment* **26** (5), 2130–2141.

Naushad, M. 2014 Surfactant assisted nano-composite cation exchanger: development, characterization and applications for the removal of toxic Pb²⁺ from aqueous medium. *Chemical Engineering Journal* **235**, 100–108.

Naushad, M. & ALOthman, Z. A. 2015 Separation of toxic Pb²⁺ metal from aqueous solution using strongly acidic cation-exchange resin: analytical applications for the removal of metal ions from pharmaceutical formulation. *Desalination and Water Treatment* **53** (8), 2158–2166.

Naushad, M., ALOthman, Z. A., Awual, M. R., Alam, M. M. & Eldesoky, G. E. 2015 Adsorption kinetics, isotherms, and thermodynamic studies for the adsorption of Pb²⁺ and Hg²⁺ metal ions from aqueous medium using Ti (IV) iodovanadate cation exchanger. *Ionics* **21** (8), 2237–2245.

Naushad, M., Ahamad, T., Al-Maswari, B. M., Alqadami, A. A. & Alshehri, S. M. 2017 Nickel ferrite bearing nitrogen-doped mesoporous carbon as efficient adsorbent for the removal of highly toxic metal ion from aqueous medium. *Chemical Engineering Journal* **330**, 1351–1360.

Pugazhendhi, A., Boovaragamoorthy, G. M., Ranganathan, K., Naushad, M. & Kaliannan, T. 2018 New insight into effective biosorption of Pb²⁺ from aqueous solution using Ralstonia solanacearum: characterization and mechanism studies. *Journal of Cleaner Production* **174**, 1234–1239.

Qi, Y. C., Shen, J., Jiang, Q. Y., Jin, B., Chen, J. W., Zhang, X. & Su, J. L. 2016 Hierarchical porous hydroxyapatite microspheres: synthesis and application in water treatment. *Journal of Materials Science* **51**, 2598–2607.

Rimola, A., Corno, M., Zicovich-Wilson, C. M. & Ugliengo, P. 2008 Ab initio modeling of protein/biomaterial interactions: glycine adsorption at hydroxyapatite surfaces. *Journal of the American Chemical Society* **130**, 16181–16183.

Snihirova, D., Lamaka, S. V., Taryba, M., Salak, A. N., Kallip, S., Zheludkevich, M. L., Ferreira, M. G. S. & Montemor, M. F. 2010 Hydroxyapatite microparticles as feedback-active reservoirs of corrosion inhibitors. *ACS Applied Materials & Interfaces* **2** (11), 3011–3022.

Vila, M., Sánchezsalcedo, S., Cicuéndez, M., Izquierdo-Barba, I. & Vallet-Regí, M. 2011 Novel biopolymer-coated hydroxyapatite foams for removing heavy-metals from polluted water. *Journal of Hazardous Materials* **192** (1), 71–77.

Wang, D. D., Guan, X. M., Huang, F. Z., Li, S. K., Shen, Y. H., Chen, J. & Long, H. B. 2016 Removal of heavy metal ions by biogenic hydroxyapatite: morphology influence and mechanism study. *Russian Journal of Physical Chemistry A* **90** (8), 1557–1562.

Wang, J. F., Qian, W. Z., He, Y. F., Xiong, Y. B., Song, P. F. & Wang, R.-M. 2017 Reutilization of discarded biomass for preparing functional polymer materials. *Waste Management* **65**, 11–21.

Wang, Y., She, H. D., Ma, Q., Lian, J. H., Zhong, J. B., Li, J. Z., Tong, J. H., He, Y. F., Wang, R.-M. & Wang, Q. Z. 2018 Plant-protein-modified TiO₂(SPI@TiO₂) for photodegradation of dyes. *Chemistry Select* **3** (11), 3127–3132.

Wei, X. & Matthew, Z. Y. 2012 Yttrium-doped hydroxyapatite membranes with high proton conductivity. *Chemistry of Materials* **24**, 1738–1743.

Wei, L., Wang, S. T., Zuo, Q. Q., Liang, S. X., Shen, S. G. & Zhao, C. X. 2016 Nano-hydroxyapatite alleviates the detrimental effects of heavy metals on plant growth and soil microbes in e-waste-contaminated soil. *Environmental Science-Processes & Impacts* **18** (6), 760–767.

Wijesinghe, W. P. S. L., Mantilaka, M. M. M. G. P. G., Nirmal Peiris, T. A., Rajapakse, R. M. G., Upul Wijayantha, K. G., Pitawala, H. M. T. G. A., Premachandra, T. N., Herathg, H. M. T. U. & Rajapaksef, R. P. V. J. 2018 Preparation and characterization of mesoporous hydroxyapatite with non-cytotoxicity and heavy metal adsorption capacity. *New Journal of Chemistry* **42** (12), 10271–10278.

Zhang, Y. G., Zhu, Y. J., Chen, F. & Sun, T. W. 2017 Biocompatible, ultralight, strong hydroxyapatite networks based on hydroxyapatite microtubes with excellent permeability and ultralow thermal conductivity. *ACS Applied Materials & Interfaces* **9**, 7918–7928.

Zhu, Y., Yang, Q., Yang, M. G., Zhan, X. H., Lan, F., He, J., Gu, Z. W. & Wu, Y. 2017 Protein corona of magnetic hydroxyapatite scaffold improves cell proliferation via activation of mitogen-activated protein kinase signaling pathway. *ACS Nano* **11**, 3690–3704.